

# 1 Inter-annual surface evolution of an Antarctic blue-ice moraine 2 using multi-temporal DEMs

3  
4 **Matthew J. Westoby<sup>1</sup>, Stuart A. Dunning<sup>2</sup>, John Woodward<sup>1</sup>, Andrew S. Hein<sup>3</sup>, Shasta  
5 M. Marrero<sup>3</sup>, Kate Winter<sup>1</sup> and David E. Sugden<sup>3</sup>**

6  
7 [1]{Department of Geography, Engineering and Environment, Northumbria University,  
8 Newcastle upon Tyne, UK}

9  
10 [2]{School of Geography, Politics and Sociology, Newcastle University, Newcastle upon  
11 Tyne, UK}

12  
13 [3]{School of GeoSciences, University of Edinburgh, Edinburgh, UK}

14  
15 Correspondence to: M. J. Westoby (matt.westoby@northumbria.ac.uk)

## 16 17 **Abstract**

18  
19 Multi-temporal and fine resolution topographic data products are increasingly used to  
20 quantify surface elevation change in glacial environments. In this study, we employ  
21 3D digital elevation model (DEM) differencing to quantify the topographic evolution of  
22 a blue-ice moraine complex in front of Patriot Hills, Heritage Range, Antarctica.  
23 Terrestrial laser scanning (TLS) was used to acquire multiple topographic datasets of  
24 the moraine surface at the beginning and end of the austral summer season in  
25 2012/2013 and during a resurvey field campaign in 2014. A complementary  
26 topographic dataset was acquired at the end of season 1 through the application of  
27 Structure-from-Motion with multi-view stereo (SfM-MVS) photogrammetry to a set of  
28 aerial photographs acquired from an unmanned aerial vehicle (UAV). Three-  
29 dimensional cloud-to-cloud differencing was undertaken using the Multiscale Model  
30 to Model Cloud Comparison (M3C2) algorithm. DEM differencing revealed net uplift  
31 and lateral movement of the moraine crests within season 1 (mean uplift ~0.10 m),  
32 and surface lowering of a similar magnitude in some inter-moraine depressions and  
33 close to the current ice margin, although we are unable to validate the latter. Our  
34 results indicate net uplift across the site between seasons 1 and 2 (mean 0.07 m).  
35 This research demonstrates that it is possible to detect dynamic surface  
36 topographical change across glacial moraines over short (annual to intra-annual)  
37 timescales through the acquisition and differencing of fine-resolution topographic  
38 datasets. Such data offer new opportunities to understand the process linkages  
39 between surface ablation, ice flow, and debris supply within moraine ice.

## 40 1. Introduction

41

42 Fine-resolution topographic data products are now routinely used for the  
43 geomorphometric characterisation of Earth surface landforms (e.g. Passalacqua et  
44 al., 2014, 2015; Tarolli, 2014). Recent decades have seen the advent and uptake of  
45 a range of surveying technologies for characterising the form and evolution of Earth  
46 surface topography at the macro- (landscape; kilometres), meso- (landform; metres)  
47 and micro-scales (patch-scale; centimetre-millimetre). These technologies have  
48 included, amongst others, the use of satellite remote sensing techniques (e.g. Kääb,  
49 2002; Smith et al., 2006; Farr et al., 2007; Stumpf, 2014; Noh and Howat, 2015), as  
50 well as field-based surveying platforms such as electronic distance meters (total  
51 station; e.g. Keim et al., 1999; Fuller et al., 2003), differential global positioning  
52 systems (dGPS; e.g. Brasington et al., 2000; Wheaton et al., 2010), terrestrial laser  
53 scanning (TLS; e.g. Rosser et al., 2005; Hodge et al., 2009), airborne light detection  
54 and ranging (LiDAR; e.g. Bollmann et al., 2011) and softcopy or digital  
55 photogrammetry (e.g. Micheletti et al., 2015).

56

57 More recently, geoscientists are increasingly adopting low-cost Structure-from-  
58 Motion with multi-view stereo (SfM-MVS) methods, which employ computer vision  
59 and multi-view photogrammetry techniques to recover surface topography using  
60 optical (e.g. James and Robson, 2012; Westoby et al., 2012; Javernick et al., 2014;  
61 Micheletti et al., 2014; Woodget et al., 2015; Smith and Vericat, 2015) or thermal  
62 imagery (e.g. Lewis et al., 2015). Concomitant developments in lightweight  
63 unmanned aerial vehicle (UAV) technology, specifically decreasing system costs,  
64 increased portability, and improvements in the accessibility of flight planning  
65 software have encouraged the acquisition of repeat, fine-resolution (metre to  
66 centimetre) topographic data products from low-altitude aerial photography platforms  
67 (e.g. Niethammer et al., 2010; Ouédraogo et al., 2014; Bhardwaj et al., 2016).  
68 Furthermore, the differencing of topographic datasets acquired at different times is  
69 now an established method for quantifying the transfer of mass and energy through  
70 landscapes at the spatial scales of observation at which many processes operate  
71 (Passalacqua et al., 2015).

72

73 Fine-resolution topographic datasets produced using airborne or ground-based light  
74 detection and ranging (LiDAR), or terrestrial or low-altitude aerial digital  
75 photogrammetry have been used for a diverse range of applications in various  
76 glacial, proglacial, and periglacial environments at a range of scales, including: the  
77 quantification of ice surface evolution (e.g. Baltsavias et al., 2001; Pitkänen and  
78 Kajuutti, 2004; Keutterling and Thomas, 2006; Schwalbe and Maas, 2009;

79 Immerzeel et al., 2014; Pepin et al., 2014; Whitehead et al., 2014; Gabbud et al.,  
80 2015; Kraaijenbrink et al., 2015; Piermattei et al., 2015; Ryan et al., 2015); mapping  
81 the redistribution of proglacial sediment (e.g. Milan et al., 2007; Irvine-Fynn et al.,  
82 2011; Dunning et al., 2013; Staines et al., 2015) and moraine development  
83 (Chandler et al., 2015); the characterisation of glacier surface roughness (e.g. Sanz-  
84 Ablanedo et al., 2012; Irvine-Fynn et al., 2014), glacial sedimentology (Westoby et  
85 al., 2015), and hydrology (Rippin et al., 2015); as well as input data for surface  
86 energy balance modelling (e.g. Arnold et al., 2006; Reid et al., 2012); and for  
87 characterising glacial landforms in formerly glaciated landscapes (e.g. Smith et al.,  
88 2009; Tonkin et al., 2014; Hardt et al., 2015).

89

90 In this study, we utilise fine-resolution topographic datasets to quantify the surface  
91 evolution of a blue-ice moraine complex in a remote part of Antarctica. Blue-ice  
92 areas cover approximately 1% of Antarctica's surface area (Bintanja, 1999), yet they  
93 remain relatively understudied. Relict blue-ice moraines preserved on nunataks are  
94 key indicators of ice sheet elevation changes; however, limited data exist on rates  
95 and patterns of surface reorganisation, which may be of use for contextualising the  
96 results of, for example, cosmogenic nuclide dating and geomorphological mapping  
97 (Hein et al., 2016). This research seeks to quantify the short-term surface evolution  
98 of a moraine complex in Patriot Hills, Heritage Range, Antarctica (Fig. 1), through the  
99 differencing and analysis of multi-temporal topographic datasets acquired using TLS  
100 and the application of SfM-MVS photogrammetry to optical imagery acquired from a  
101 low-altitude UAV sortie.

102

## 103 **2. Study site**

104

105 The study site is a blue-ice moraine complex, located on the northern flank of the  
106 Patriot Hills massif at the southern-most extent of Heritage Range, West Antarctica  
107 (Fig. 1). Blue-ice moraine formation is hypothesised to be the result of preferential  
108 ablation of marginal ice by katabatic winds, which in turns prompts the modification  
109 of ice flow and englacial sediment transport pathways such that basal sediment is  
110 brought to the ice surface, where it is deposited (e.g. Bintanja, 1999; Sinisalo and  
111 Moore, 2010; Fogwill et al., 2012; Spaulding et al., 2012; Hein et al., 2016). The site  
112 comprises a series of broadly east-west oriented moraine ridges and inter-moraine  
113 troughs, as well as an area of subdued moraine topography immediately adjacent to  
114 the ice margin (Fig. 2). At this location, the active blue-ice moraines occupy an  
115 altitudinal range of 60-70 m above the ice margin (~730 m a.s.l.) and extend for a  
116 distance of up to 350 m into a bedrock embayment (Fig. 1). The blue-ice moraines  
117 can be traced for a distance of >4 km to the east and north-east, parallel to the range

118 front, and fill ice-marginal embayments. The site is geomorphologically and  
119 sedimentologically complex (e.g. Vieira et al., 2012; Westoby et al., 2015), and,  
120 along with moraine ridges and troughs, includes areas of subdued ice-marginal  
121 topography with thermokarst melt ponds, local gullying and crevassing on ice-  
122 proximal and distal moraine flanks, as well as solifluction deposits at the base of the  
123 surrounding hillslopes. The bedrock hillslopes are overlain by a till drape with rare,  
124 large exotic sandstone boulder erratics which have some evidence of periglacial  
125 reworking. Field observations suggest that the blue-ice moraines are dynamic  
126 features which are undergoing localised surface changes. It is these short-term,  
127 changes which are the subject of investigation in this paper.

128

### 129 **3. Methods and data products**

130

131 This research employs two methods for reconstructing moraine surface topography,  
132 specifically TLS and SfM-MVS photogrammetry. Two field campaigns at Patriot Hills  
133 were undertaken with a 12-month survey interval. Briefly, TLS data were acquired at  
134 the beginning and end of austral summer season 1 (December 2012 and January  
135 2013, respectively), and in a short resurvey visit in season 2 (January 2014). Low-  
136 altitude aerial optical photography was acquired from a UAV at the end of season 1  
137 and was used as the primary input to SfM-MVS processing. The following sections  
138 detail the two methods of topographic data acquisition, data processing, and  
139 subsequent analysis using cloud-to-cloud differencing.

140

#### 141 **3.1. Topographic data acquisition**

142

##### 143 **3.1.1. Terrestrial Laser Scanning**

144

145 TLS data were acquired using a Riegl LMS-Z620 time-of-flight laser scanner, set to  
146 acquire ~11,000 points per second in the near-infrared band at horizontal and  
147 vertical scanning increments of  $0.031^\circ$ , equivalent to a point spacing of 0.05 m at a  
148 distance of 100 m and with a beam divergence of 15 mm per 100 m. Data were  
149 acquired from six locations across the site at the beginning of season 1 (7<sup>th</sup> -11<sup>th</sup>  
150 December 2012; Fig. 1; Table 1). Two of these positions were re-occupied at the  
151 end of season 1 (9<sup>th</sup> January 2013) and three positions were reoccupied in season 2  
152 (Fig. 1; 14<sup>th</sup> January 2014). Following manual editing and the automated removal of  
153 isolated points to improve data quality, each set of scans were co-registered in Riegl  
154 RiSCAN PRO software (v. 1.5.9) using a two-step procedure employing coarse  
155 manual point-matching followed by the application of a linear, iterative, least-squares  
156 minimisation solution to reduce residual alignment error. Individual scans were then

157 merged to produce a single 3D point cloud for each scan date. Merged scan data  
158 from the end of seasons 1 and 2 were subsequently registered to the scan data from  
159 the beginning of season 1 using the methods described above (Table 1).

160

### 161 **3.1.2. Structure-from-Motion with multi-view stereo photogrammetry**

162

163 Low-altitude aerial photographs of the study site were acquired using a 10-Megapixel  
164 Panasonic Lumix DMC-LX5 compact digital camera with a fixed focal length (8 mm)  
165 and automatic exposure settings, mounted in a fixed, downward-facing (nadir)  
166 perspective on a sub-5 kg fixed-wing UAV. Photographs were acquired in a single  
167 sortie lasting ~5 minutes. A total of 155 photographs were acquired at a 2-second  
168 interval at an approximate ground height of 120 m, producing an average image  
169 overlap of 80%, and an approximate ground resolution of 0.07 m<sup>2</sup> per pixel. Mean  
170 point density was ~300 points per m<sup>2</sup>, compared to a mean of 278 points per m<sup>2</sup> for  
171 the TLS datasets. Motion blur of the input images was negligible due to favourable  
172 image exposure conditions and an appropriate UAV flying height and speed.

173

174 UAV photographs were used as input to SfM reconstruction using the proprietary  
175 Agisoft PhotoScan Professional Edition (v. 1.1.6) software. Unique image tie-points  
176 which are stable under variations in view perspective and lighting are identified and  
177 matched across input photographs, similar to Lowe's (2004) Scale Invariant Feature  
178 Transform (SIFT) method. An iterative bundle adjustment algorithm is used to solve  
179 for internal and external camera orientation parameters and produce a sparse 3D  
180 point cloud. The results of the first-pass camera pose estimation were scrutinised  
181 and only 3D points which appear in a minimum of 3 photographs and possessed a  
182 reprojection error of <1.0 were retained. A two-phase method of UAV-SfM data  
183 registration was employed: 1) ground control was obtained by identifying common  
184 features in the UAV-SfM photographs and TLS data from the end of season 1  
185 (acquired 4 days after the SfM data; Table 1), such as the corners of large, well-  
186 resolved boulders or bedrock outcrops. GCP data were used to optimise the initial  
187 camera alignment and transform the regenerated UAV-SfM data to the same object  
188 space as the TLS data, producing an xyz RMS error of 0.23 m. 2) following dense  
189 reconstruction using Multi-View Stereo methods, 3D point data were exported to  
190 RiSCAN PRO (v. 1.5.9) software, and a linear, iterative, least-squares minimisation  
191 employing surface plane matching was used to improve the alignment and reduce  
192 the xyz RMS error to 0.03 m.

193

### 194 **3.2. Cloud-to-cloud differencing**

195

196 Three-dimensional cloud-to-cloud distance calculations were used to quantify  
197 moraine surface evolution (e.g. Lague et al., 2013). Since the dominant direction of  
198 surface evolution across the study site was unknown *a priori*, the application of an  
199 algorithm that is capable of detecting fully three-dimensional topographic change  
200 was deemed to be the most appropriate method in this context. To this end, we  
201 employ the Multiscale Model to Model Cloud Comparison (M3C2) algorithm (Lague  
202 et al., 2013; Barnhart and Crosby, 2013), implemented in the open-source  
203 CloudCompare software (v. 2.6.1) for change detection.

204

205 The M3C2 algorithm implements two main processing steps to calculate 3D change  
206 between two point clouds: 1) estimation of surface normal orientation at a scale  
207 consistent with local surface roughness, and 2) quantification of the mean cloud-to-  
208 cloud distance (i.e. surface change) along the normal direction (or orthogonal  
209 vector), which includes an explicit calculation of the local confidence interval. A point-  
210 specific normal vector is calculated by fitting a plane to neighbouring 3D points that  
211 are contained within a user-specified search radius. To avoid the fluctuation of  
212 normal vector orientations and a potential overestimation of the distance between  
213 two point clouds, the radius, or scale, used for normal calculation needs to be larger  
214 than the topographic roughness, which is calculated as the standard deviation of  
215 local surface elevations ( $\sigma$ ). The orientation of the surface normal around a point,  $i$ , is  
216 therefore dependent on the scale at which it is computed (Lague et al., 2013). A trial-  
217 and-error approach was employed to reduce the estimated normal error,  $E_{\text{norm}}(\%)$ ,  
218 through refinement of a re-scaled measure of  $D$ ,  $\xi$ , where:

219

$$220 \quad \xi(i) = \frac{D}{\sigma_i(D)} \quad \text{Eq. (1)}$$

221

222 Using this re-scaled measure of  $D$ ,  $\xi$  can be used as an indicator of estimated normal  
223 orientation accuracy, such that where  $\xi$  falls in the range  $\sim 20$ -25, the estimated  
224 normal error is  $E_{\text{norm}} < 2\%$  (Lague et al., 2013). A fixed normal scaling of 2 m was  
225 found to be sufficient to ensure that  $\xi > 20$  for  $>98\%$  of points in each topographic  
226 dataset.

227

228 The radius of the projection cylinder,  $d$ , within which the average surface elevation of  
229 each cloud is calculated, was specified as 2 m. This scaling ensured that the number  
230 of points sampled in each cloud was  $\geq 30$ , following guidance provided by Lague et  
231 al. (2013). M3C2 execution took  $\sim 0.3$  h for each differencing task on a desktop  
232 computer operating with 32 GB of RAM, and a 3.4 GHz CPU. Cloud-to-cloud  
233 distances and statistics were projected onto the original point cloud. M3C2 output

234 was subsequently masked to exclude points where change is lower than level of  
235 detection threshold for a 95% confidence level,  $LoD_{95\%}(d)$ , which is defined as:

236

$$237 \quad LoD_{95\%}(d) = \pm 1.96 \left( \frac{\sigma_1(d)^2}{n_1} + \frac{\sigma_2(d)^2}{n_2} + reg \right) \quad \text{Eq. (2)}$$

238

239 where  $d$  is the radius of the projection cylinder,  $reg$  is the user-specified registration  
240 error, for which we substitute the propagated root mean square alignment error for  
241 point clouds  $n_1$  and  $n_2$  (Table 2; Eq. (1)) and assume that this error is isotropic and  
242 spatially uniform across the dataset.

243

244 To calculate the total propagated error for each differencing epoch,  $\sigma_{DoD}$ , the  
245 estimates of errors in each point cloud (i.e. the sum of the average scan-scan RMS  
246 error and a project-project RMS error, where applicable) were combined using:

247

$$248 \quad \sigma_{DoD} = \sqrt{\sigma_{C_1}^2 + \sigma_{C_2}^2} \quad \text{Eq. (3)}$$

249

250 where  $\sigma_{C_1}^2$  and  $\sigma_{C_2}^2$  are the RMS errors associated with point clouds  $C_1$  and  $C_2$ .

251

252

### 253 **3.3. Data intercomparison: SfM vs. TLS**

254

255 Whilst the UAV-SfM dataset acquired at the end of season 1 significantly improves  
256 on the spatial coverage afforded by the use of TLS across the moraine embayment,  
257 an analysis of the relative accuracy of the reconstructed surface topography of the  
258 former is required. To this end, Fig. 3 shows the results of vertical differencing of the  
259 UAV-SfM and TLS data and is complemented by a series of surface elevation  
260 profiles (Fig. 4). These results reveal that 83% of the UAV-SfM data are within  $\pm 0.1$   
261 m of the equivalent TLS data when gridded as the mean of vertical displacement in  
262  $10 \text{ m}^2$  grid cells.

263

264 However, two zones of substantial vertical discrepancy exist, namely the  
265 northernmost (ice-marginal) sector of the site, where the UAV-SfM data locally  
266 underestimate the equivalent TLS surface elevation by  $< -0.20$  m (mean  $-0.13$  m),  
267 and a zone to the north-west of the site, where the UAV-SfM data locally  
268 overestimate the TLS ground surface elevation by  $> 0.20$  m (mean  $0.12$  m). We  
269 propose two explanations for these vertical discrepancies. Firstly, it was difficult to  
270 identify corresponding features in the TLS and UAV-SfM datasets in the north-  
271 western sector of the site due to the sparsity of TLS data coverage here at the end of

272 season 1 (*cf.* Fig. 5c and Fig. 5d). Secondly, the UAV executed sharp banking turns  
273 in this area of the site to clear a hillslope spur. These manoeuvres were difficult for  
274 the on-board camera stabilising gimbal to compensate for, thereby reducing the  
275 effective side- and forward overlap of the aerial photography, Similar banking turns  
276 were carried out at the eastern edge of the site, however, it was possible to more  
277 confidently identify GCPs in the TLS data in this region, which appears to have had a  
278 mitigating effect against the effects of reduced image overlap on scene  
279 reconstruction. Finally, those features that did appear in the TLS data in this sector  
280 were typically near-vertical faces of large clasts which were oriented toward the  
281 scanner, and which were not well-resolved in the UAV-SfM data due to its nadir  
282 perspective. This made the accurate identification of matching clast features or  
283 edges challenging. Ultimately, we attribute less confidence in both the geometric  
284 accuracy of the 3D SfM-MVS reconstruction and final model-to-model alignment in  
285 the north-western sector of the site.

286

287 We attribute underestimated UAV-SfM surface elevations in the centre-north of the  
288 site to also be a product of the differing spatial extents of the two datasets. In this  
289 location, the northernmost extent of the UAV-SfM data encompasses the entire ice-  
290 marginal zone, whereas the equivalent TLS data were truncated at the foot of the  
291 main moraine crest due to logistical constraints which precluded the acquisition of a  
292 more complete TLS dataset at the end of season 1. Since no robust GCPs could be  
293 identified in the TLS data for the ice-marginal zone for use in the UAV-SfM camera  
294 optimisation and registration process, the ground surface geometry in this area tends  
295 towards a systematic negative elevation bias, possibly as the result of residual radial  
296 lens distortion following camera calibration in PhotoScan (e.g. James and Robson,  
297 2014), we were unable to compensate for.

298

299 Transect data also highlight areas of inconsistency, specifically often considerable  
300 offsets between the TLS and SfM data which were collected at the end of season 1  
301 and which, in places, approach 0.5 m in magnitude (e.g. at ~27 m distance in profile  
302 A, and between 22-30 m in profile B; Fig. 4). An additional explanation for these  
303 inconsistencies could be the evolution of moraine surface topography in the 4-day  
304 interval which separated the acquisition of the TLS and SfM data at the end of  
305 season 1 (Table 1), with the implication that features used as GCPs in the TLS data  
306 and their counterparts in the UAV-SfM data were not static, thereby affecting the  
307 georeferencing and SfM optimisation solution. However, since we observed no  
308 clustering of large GCP errors in areas of activity, as shown in the TLS-TLS  
309 differencing results, this factor is unlikely to account for these topographic  
310 inconsistencies.



311

312 Topographic mismatches between the TLS and UAV-SfM data also appear to be the  
313 most prominent in areas of steep topography (Fig. 3; Fig. 4). These areas were  
314 generally well-resolved in the TLS data (where not topographically occluded), but  
315 may have been resolved in less detail and with less accuracy in the UAV-SfM data,  
316 where the fixed camera angle promotes the foreshortening of these steep slopes in  
317 the aerial photography. These differences might also be explained by the near-  
318 parallel and largely nadir view directions of the UAV imagery, which represent a  
319 'non-convergent' mode of photograph acquisition that has elsewhere been found to  
320 result in the deformation, or 'doming' of SfM-derived surface topography (e.g. James  
321 and Robson, 2014; Rosnell and Honkavaara, 2012; Javernick et al., 2014).

322

323 Model deformations can be countered to some degree through the inclusion of  
324 additional, oblique imagery, and the use of a well-distributed and photo-visible GCP  
325 network (James and Robson, 2014). However, although the latter were relatively  
326 evenly distributed across our study site, the inclusion of these data and subsequent  
327 use for the optimisation of the SfM data prior to dense point cloud reconstruction  
328 does not appear to have altogether eliminated these model deformations. We  
329 discuss the implications of data quality issues for interpreting geomorphological  
330 process analysis in sections 4 and 5.

331

## 332 **4. Short-term topographic evolution of blue-ice moraines**

333

### 334 **4.1. Vertical displacement**

335

336 The results of 3D cloud-to-cloud differencing are summarised in Figure 5. Threshold  
337 levels of change detection ranged from 0.094 – 0.103 m. The upper (i.e. most  
338 conservative) bound of this range was applied to the results from all differencing  
339 epochs, so that only 3D surface change greater than  $\pm 0.103$  m was considered in  
340 the subsequent analysis. The horizontal ( $xy$ ) and vertical ( $z$ ) components of 3D  
341 surface change were separated to aid the analysis and interpretation of moraine  
342 surface evolution and were gridded to represent the mean of significant change  
343 within regular  $10\text{ m}^2$  grid cells to account for variations in point density across the  
344 site (Fig. 5, Fig. 6). Vertical surface change for a range of epochs, encompassing  
345 intra-annual and annual change, are displayed in Fig. 5, whilst illustrative horizontal  
346 components of 3D change for intra- and inter-annual differencing epochs are shown  
347 in Fig. 6. The longest differencing epoch, representing a period of  $\sim 400$  days (Fig.  
348 5b) shows a broad pattern of net uplift across the moraine of the order of 0.074 m.  
349 Locally, uplift exceeds 0.2 m across parts of the moraine complex, and, whilst on first  
350 glance these elevation gains appear to be largely randomly distributed across the  
351 site, on closer inspection they occur predominantly on or adjacent to the main,

352 central moraine ridge and close to the current ice margin. The large central moraine  
353 ridge exhibits a mean uplift of 0.11 m, whilst specific ice-marginal areas to the west  
354 and an area of moraine to the south-west of the embayment also exhibit uplift of a  
355 similar magnitude (Fig. 5b). In contrast, an area in the southernmost sector of the  
356 basin and an ice-marginal area to the centre-west exhibit a net reduction in moraine  
357 surface elevation, up to a maximum of -0.354 m.

358

359 Intra-annual change detection mapping was undertaken using TLS-TLS and TLS-  
360 SfM differencing (Fig. 5c, d). Key similarities between these two datasets, which  
361 represent vertical topographic change over a ~31 and ~27 day period, respectively,  
362 include uplift at the southern extent of the embayment (mean 0.081 m and 0.123 m  
363 for the TLS-TLS and TLS-SfM differencing, respectively). Similarly, both datasets  
364 reveal surface lowering at south-eastern, or true rear, of the basin (mean -0.106 m  
365 and -0.112 m for TLS-SfM and TLS-TLS differencing, respectively), and, in the TLS-  
366 SfM data, on the ice-distal (southern) side of the central moraine ridge (Fig. 5c; -  
367 0.092 m). However, the large area of ice-marginal surface lowering (-0.095 - -0.373  
368 m) that is detected in the TLS-SfM differencing results is not mirrored in the  
369 equivalent TLS-TLS differencing data (Fig. 5d) and stems in large part from the  
370 reduced spatial coverage of the usable TLS scan data acquired at the end of season  
371 1, which comprised data from only two scan positions (Fig. 1c) and which omits the  
372 ice-marginal zone.

373

374 The results of vertical change detection using both SfM-TLS and TLS-TLS  
375 approaches also display similarities for differencing undertaken between the end of  
376 season 1, and season 2 (Fig. 5e,f), including a largely continuous area of uplift  
377 across the centre of the site, as well as areas of surface lowering along the eastern  
378 edge of the site. Whilst widespread uplift characterises the entire western edge of  
379 the study area in the TLS-TLS data (Fig. 5f), the equivalent SfM-TLS data instead  
380 report the occurrence of surface lowering at the base of the hillslope spur which  
381 forms the western boundary of the site (Fig. 5e). Furthermore, an area of  
382 considerable (mean 0.218 m) uplift characterises the ice-marginal zone in the SfM-  
383 TLS differencing data for this epoch, but, once again, the reduced spatial coverage  
384 of the TLS datasets mean that no differencing data are available to verify or contest  
385 this pattern. However, we note that vertical change at the ice-marginal (northern)  
386 limit of the TLS-TLS data for both intra-annual and annual differencing epochs do not  
387 correspond with the equivalent TLS-SfM or SfM-TLS results (Fig. 5c and 5e,  
388 respectively).

389

390 In light of our discussion of the sources of substantial topographic discrepancy  
391 between the TLS and UAV-SfM datasets (Fig. 3; section 3.3), important questions  
392 arise as to whether the differencing results in the ice-marginal zone, and in the  
393 western sector of the site truly represent physical surface movement, both within  
394 season 1, and between seasons (Fig. 5, 6). On balance, and despite the application  
395 of a sufficiently large confidence threshold to remove non-significant change from the  
396 differencing results (Table 2), we retain much less confidence in reported surface  
397 displacement in these two zones than we do for the central portion and rear arc of  
398 the moraine basin, where we note that the results of TLS-SfM and TLS-TLS  
399 differencing for near-identical differencing periods exhibit a number of similarities.

400

#### 401 **4.2. Lateral displacement**

402

403 Examples of horizontal displacement, calculated here as the  $xy$  component of the  
404 orthogonal distance between two point clouds acquired at separate times, and  
405 gridded to represent the average  $xy$  displacement within  $10\text{ m}^2$  grid cells, are shown  
406 in Fig. 6 for intra- (Fig. 6a,b) and inter-annual epochs (Fig. 6c). A range of  $xy$   
407 displacement orientations are detected, and range from sub-centimetre to  $>0.2\text{ m}$  in  
408 magnitude. Lateral displacements within season 1 are displayed for both TLS-TLS  
409 and TLS-SfM differencing products (Fig. 6a and 6b, respectively).

410

411 A comparison of these two datasets reveal similarities, but also differences which  
412 also likely arise from data quality issues in the north-west and ice-marginal sectors of  
413 the site. Specifically, we cannot confidently corroborate the southerly displacement  
414 vectors which are associated with substantial, yet questionable, ice-marginal surface  
415 lowering in the TLS-SfM data (Fig. 6b). Similarly, the sparsity of TLS data coverage  
416 in the western sector of the site makes validation of the northerly vectors associated  
417 with surface uplift in the western sector of the site problematic. However, we note  
418 that a similar pattern of vertical and lateral displacement is present in the inter-  
419 annual TLS-TLS results in the western sector of the site (Fig. 6c), and so it remains  
420 unclear as to whether this surface displacement is an artefact produced by poor data  
421 quality. Elsewhere in the embayment, lateral displacements within season 1 exhibit  
422 similarities between both sets of differencing data, including a dominantly westward  
423 trajectory of surface movement, and a localised area of south- to south-westerly  
424 movement at the extreme rear of the basin which is associated with a general  
425 pattern of surface lowering in both datasets (Fig. 6a, 6b).

426

427 In contrast, total  $xy$  displacement over a  $>1$  year period (Fig. 6c) appears to be less  
428 uniform and comparatively chaotic. However, a number of local and largely

429 consistent patterns of horizontal displacement are discernible, such as  
430 predominantly westward movement along the central moraine ridge, and north- to  
431 north-eastern motion along the western edge of the site (Fig. 6c), which also occurs  
432 within season 1 (Fig. 6a). Both trends are associated with net surface uplift. In  
433 contrast, isolated patches of surface lowering are generally characterised by  
434 southern or south-westerly xy displacement.

435

436 The analysis of surface profile transects shed further light on the evolution of surface  
437 topography (Fig. 4). These data are particularly useful for examining the interplay  
438 between vertical and lateral moraine surface displacement, which is alluded to in Fig.  
439 6. For example, a combination of surface uplift and lateral displacement between the  
440 start and end of season 1 is visible between 28-40 m in profile A (Fig. 4, inset 1).  
441 Similarly, lateral (southern) translation of the moraine surface between 15-22 m in  
442 profile C (Fig. 4, inset 2) is visible for the same differencing epoch.

443

## 444 **5. Implications for glaciological process analysis**

445

446 Here we highlight some implications arising from the measurement of these short-  
447 term changes in surface morphology. Topographically, the Patriot Hills blue-ice  
448 moraine confirms the morphological observations of the embayment, described by  
449 Fogwill et al. (2012) as comprising sloping terraces and blocky, pitted boulder  
450 moraine ridges. These ridges are thought to be fed from beneath by steeply dipping  
451 debris bands coming from depth, driven by ice-flow compensating for katabatic wind  
452 ablation of the glacier. Vieira et al. (2012) classify what we term blue-ice moraines as  
453 'supraglacial moraine', and the debris bands in the blue ice outside of the basin as  
454 blue-ice moraines. It is from clasts emerging from these bands that Fogwill et al.  
455 (2012) have produced their model of blue-ice moraine formation in the basin. The  
456 supraglacial moraines of Vieira et al. (2012) are described as slightly creeping  
457 debris-mantled slopes – both Fogwill et al. (2012) and Vieira et al. (2012) consider  
458 the features in the basin as active, but without measurements of observations of  
459 rates, or the nature of change. Our differencing results confirm the hypothesis that  
460 these features are active, and develops this idea further to demonstrate that moraine  
461 slope evolution is active over annual to intra-annual timescales.

462

463 Hättestrand and Johansen (2005) discussed the evolution of blue-ice moraine  
464 complexes in Dronning Maud Land, Antarctica, and hypothesised that, following ice-  
465 marginal deposition of debris when the adjacent ice surface was higher, the  
466 subsequent lowering of the exposed ice surface would produce a slope 'outwards'  
467 from an embayment, followed by gradual movement of material towards the ice-

468 margin in a manner similar to that exhibited by active rock glaciers – features that  
469 Vieira et al. (2012) interpret in the next basin along the Patriot Hills range. However,  
470 whilst the former holds true as an explanation for the general gradient of the Patriot  
471 Hills moraine complex (e.g. Fig. 4), our results suggest that the short-term evolution  
472 of the moraines does not necessarily conform to the latter hypothesis of such as  
473 simple process of consistent downslope movement, and in fact exhibits far more  
474 dynamic complexity.

475

476 The moraine ridges both close to, and far from the ice margin emerge as axes of  
477 activity and uplift (Fig. 5c), despite initial field observations suggesting that the ridges  
478 most distant from the exposed ice surface were older and less active. However, we  
479 exercise caution in the interpretation of surface displacements in the western, and  
480 ice-marginal sectors of the site due to UAV-SfM data quality issues, and instead  
481 confine our discussion of geomorphological activity to the remaining ~50% of the  
482 basin area, where we retain confidence in the results of TLS-TLS and TLS-SfM  
483 differencing.

484

485 Fogwill et al. (2012) suggest that once upcoming debris is at a sufficient thickness,  
486 wind-driven ablation shuts off. Our observations suggest that if this is the case, these  
487 ridges are not left stagnant at this point. The interplay between ice flow and surface  
488 elevation lowering by wind, but reduced by thicker debris, may continue despite the  
489 possible ages of the surface debris relative to ridges closer to the contemporary  
490 blue-ice margin. This activity is not simply confined to '*inward*' or '*outward*'  
491 movement of moraines within the embayment, but also involves a lateral component  
492 (Fig. 6). Whilst we are unable to corroborate the substantial surface lowering  
493 reported in the TLS-SfM differencing for the ice-marginal zone within season 1 (Fig.  
494 5c) and between seasons (Fig. 5e), areas of seemingly persistent uplift are located  
495 on the ice-distal face of the central moraine ridge, as well as along moraine ridges  
496 toward the rear of the basin. These trends appear in both the TLS-SfM and TLS-TLS  
497 differencing results (Fig. 5, Fig. 6).

498

499 Similarly, surface lowering appears to operate at the rear, or southern, extent of the  
500 basin within season 1 (Fig. 5c,d) and between the beginning of season 1 and the  
501 end of season 2 (Fig. 5b). However, it is characterised by surface uplift from the end  
502 of season 1 to the end of season 2 (Fig. 5e,f). This surface lowering trend may be  
503 the product of focussed katabatic wind-driven sub-debris ice ablation, coincident with  
504 a break (reduction) in slope. There may therefore exist an interplay between moraine  
505 uplift and sub-debris ice ablation, where the latter dominates over the longest  
506 differencing period (Fig. 5b,c). Sedimentological characterisation of the moraine

507 basin by Westoby et al. (2015) revealed low median surface grain sizes toward the  
508 rear of the basin, which may be indicative of a longer sediment exposure time for, or  
509 preferential exposure to, *in situ* weathering relative to the remainder of the site,  
510 leading to the comminution of surficial deposits and the enhancement of sub-debris  
511 ice ablation, which promotes terrain relaxation (e.g. Krüger and Kjær, 2000;  
512 Schomacker, 2008; Irvine-Fynn et al., 2011; Staines et al., 2015).

513

514 Lateral movement within the moraine ridges (Fig. 6) may reflect lateral extension or  
515 'stretching' of the ridges as they encroach into the embayment. Such lateral  
516 movement is corroborated from the orientation of crevasse-based grooves in the  
517 moraine (Fig. 2c). The apparent inward encroachment of the Patriot Hills moraines  
518 (Fig. 6) may be the product of the pressure exerted on the moraines by glacier ice  
519 flow into the embayment in compensation for preferential ice ablation by katabatic  
520 winds, which is consistent with blue-ice moraine formation theory (Fogwill et al.,  
521 2012). Finally, the close match of inter-season surface elevation cross-profiles (Fig.  
522 5) points to medium-term stability of the moraine system. This conclusion will be  
523 investigated through the application of cosmogenic isotope evidence to assess  
524 change since the Holocene.

525

526 More broadly, this study has demonstrated the potential for the combination of  
527 different high-resolution surveying technologies and advanced 3D topographic  
528 differencing methods for elucidating the short-term evolution of glaciated and ice-  
529 marginal landscapes. Whilst this study has focussed on the surface evolution of  
530 Antarctic blue-ice moraines, the application of 3D differencing methods to quantify  
531 change between repeat, accurate topographic surveys has a wide range of potential  
532 glaciological applications, which cryospheric researchers have already begun to  
533 capitalise on (e.g. Piermattei et al., 2015, Gabbud et al., 2015; Kraaijenbrink et al.,  
534 2016). A key contribution of this study to the wider Earth surface dynamics  
535 community is the demonstration of truly 3D differencing methods to reveal not only  
536 vertical surface change, but also the magnitude and direction of any lateral  
537 component to surface movement. Such methods may have particular value for  
538 quantifying the 3D surface evolution of, for example, rock glaciers, degrading ice-  
539 cored moraines, or slope instabilities in permafrost regions, where information  
540 regarding both vertical and lateral components of landscape development may be  
541 both of scientific interest and practical application.

542

## 543 **6. Summary**

544

545 This research has employed a combination of TLS and UAV-based SfM-MVS  
546 photogrammetry and 3D differencing methods to quantify the topographic evolution  
547 of an Antarctic blue-ice moraine complex over annual and intra-annual timescales.  
548 Segmentation of lateral and vertical surface displacements reveal site- and local-  
549 scale patterns of geomorphometric moraine surface evolution beyond a threshold  
550 level of detection (95% confidence), including largely persistent vertical uplift across  
551 the moraine complex, both within a single season, and between seasons. This  
552 persistent uplift is interspersed with areas (and periods) of surface downwasting  
553 which is largely confined to the rear of the moraine basin for both differencing  
554 epochs, and in ice-marginal regions within season 1, the latter of which we deem as  
555 non-significant. Analysis of lateral displacement vectors, which are generally of a  
556 much smaller magnitude than vertical displacements, provide further insights into  
557 moraine surface evolution.

558

559 A number of methodological shortcomings are highlighted. Briefly, these relate to the  
560 incomplete spatial coverage afforded by the use of TLS in a topographically complex  
561 environment, and issues associated with obtaining suitable ground control for SfM-  
562 MVS processing and potential implications for the accuracy of SfM-derived  
563 topographic data products. This research represents the first successful application  
564 of a combination of high-resolution surveying methods for quantifying the  
565 topographic evolution of ice-marginal topography in this environment. Furthermore,  
566 we have demonstrated that, whilst a number of operational considerations must be  
567 taken into account at the data collection stage, these technologies are highly  
568 appropriate for reconstructing moraine surface topography and for quantifying Earth  
569 surface evolution in glaciated landscapes more generally.

570

#### 571 **Author contribution**

572

573 S. A. Dunning, J. Woodward, A. Hein, K. Winter, S. M. Marrero and D. E. Sugden  
574 collected field data. TLS and SfM data processing and differencing were undertaken  
575 by M. J. Westoby. Data analysis was performed by M. J. Westoby, S. A. Dunning  
576 and J. Woodward. Manuscript figures were produced by M. J. Westoby. All authors  
577 contributed to the writing and revision of the manuscript.

578

#### 579 **Acknowledgements**

580

581 The research was funded by the UK Natural Environment Research Council  
582 (Research Grants NE/I027576/1, NE/I025840/1, NE/I024194/1, NE/I025263/1). We  
583 thank the British Antarctic Survey for logistical support.

584 **References**

585

586 Agisoft: Agisoft PhotoScan Professional Edition v.1.1.6. Available:  
587 <http://www.agisoft.com>, 2014.

588

589 Arnold, N. S., Rees, W. G., Hodson, A. J., and Kohler, J.: Topographic controls on  
590 the surface energy balance of a high Arctic valley glacier. *Journal of Geophysical*  
591 *Research*, 111, F02011, doi: 10.1029/2005JF000426, 2006.

592

593 Baltsavias, E. P., Favey, E., Bauder, A., Bösch, H., and Pateraki, M.: Digital surface  
594 modelling by airborne laser scanning and digital photogrammetry for glacier  
595 monitoring. *Photogrammetric Record*, 17, 243-273, doi: 10.1111/0031-868X.00182,  
596 2001

597

598 Barnhart, T. B. and Crosby, B. T.: Comparing two methods of surface change  
599 detection on an evolving thermokarst using high-temporal-frequency terrestrial laser  
600 scanning, Selawik River, Alaska. *Remote Sensing*, 5, 2813-2837, doi:  
601 10.3390/rs5062813, 2013.

602

603 Bhardwaj, A., Sam, L., Akanksha, Martín-Torres, F.J., and Kumar, R.: UAVs as  
604 remote sensing platform in glaciology: Present applications and future prospects.  
605 *Remote Sensing of Environment*, 175, 196-204, doi: 10.1016/j.rse.2015.12.029,  
606 2016.

607

608 Bintanja, R.: On the glaciological, meteorological, and climatological significance of  
609 Antarctic blue ice areas. *Reviews of Geophysics*, 37, 337-359, doi:  
610 10.1029/1999RG900007, 1999.

611

612 Bollmann, E., Sailer, R., Briese, C., Stotter, J., and Fritzmann, P.: Potential of  
613 airborne laser scanning for geomorphologic feature and process detection and  
614 quantifications in high alpine mountains. *Zeitschrift für Geomorphologie*, 55, 83-104,  
615 doi: 10.1127/0372-8854/2011/0055S2-0047, 2011.

616

617 Brasington, J., Rumsby, B. T., and McVey, R. A.: Monitoring and modelling  
618 morphological change in a braided gravel-bed river using high resolution GPS-based  
619 survey. *Earth Surface Processes and Landforms*, 25, 973-990, doi: 10.1002/1096-  
620 9837(200008)25:9<973::AID-ESP111>3.0.CO;2-Y, 2000.

621

622 Chandler, B. M. P., Evans, D. J. A., Roberts, D. H., Ewertowski, M., and Clayton, A.  
623 I.: Glacial geomorphology of the Skálafellsjökull foreland, Iceland: A case study of  
624 'annual' moraines. *Journal of Maps*, doi: 10.1080/17445647.2015.1096216, 2015.

625

626 Dunning, S. A., Large, A. R. G., Russell, A. J., Roberts, M. J., Duller, R., Woodward,  
627 J., Mériaux, A-S., Tweed, F. S., and Lim, M.: The role of multiple glacier outburst  
628 floods in proglacial landscape evolution: The 2010 Eyjafjallajökull eruption, Iceland.  
629 *Geology*, 796 41(10), 1123-1136, doi: 10.1130/G34665, 2013.

630

631 Farr, T. G., Rosen, P. A., Caro, E., Crippen, R., Duren, R., Hensley, S., Kobrick, M.,  
632 Paller, M., Rodriguez, E., Roth, L., Seal, D., Shaffer, S., Shimada, J., Umland, J.,  
633 Werner, M., Oskin, M., Burbank, D., and Alsdorf, D.: The shuttle radar topography



634 mission. *Reviews of Geophysics*, 45(2), RG2004, doi: 10.1029/2005RG000183,  
635 2007.

636

637 Fogwill, C. J., Hein, A. S., Bentley, M. J., and Sugden, D. E.: Do blue-ice moraines in  
638 the Heritage Range show the West Antarctic ice sheet survived the last interglacial?  
639 *Palaeogeography, Palaeoclimatology, Palaeoecology*, 335-336, 61-70, doi:  
640 10.1016/j.palaeo.2011.01.027, 2012.

641

642 Fuller, I. C., Large, A. R. G., and Milan, D.: Quantifying channel development and  
643 sediment transfer following chute cutoff in a wandering gravel-bed river.  
644 *Geomorphology*, 54, 307-323, doi: 10.1016/S0169-555X(02)00374-4, 2003.

645

646 Gabbud, C., Micheletti, N., and Lane, S. N.: Lidar measurement of surface melt for a  
647 temperate Alpine glacier at the seasonal and hourly scales. *Journal of Glaciology*,  
648 61(229), 963-974, doi: 10.3189/2015JoG14J226, 2015.

649

650 Hardt, J., Hebenstreit, R., Lüthgens, C., and Böse, M.: High-resolution mapping of  
651 ice-marginal landforms in the Barnim region, northeast Germany. *Geomorphology*,  
652 250, 41-52, doi: 10.1016/j.geomorph.2015.07.045, 2015.

653

654 Hättestrand, C., and Johansen, N.: Supraglacial moraines in Scharffenbergbotnen,  
655 Heimafjella, Dronning Maud Land, Antarctica – significance for reconstructing  
656 former blue ice areas. *Antarctic Science*, 17(2), 225-236, doi:  
657 10.1017/S0954102005002634, 2005.

658

659 Hein, A.S., Woodward, J., Marrero, S.M., Dunning, S.A., Steig, E.J., Freeman,  
660 S.P.H.T., Stuart, F.M., Winter, K., Westoby, M.J., and Sugden, D.E.: Evidence for  
661 the stability of the West Antarctic Ice Sheet divide for 1.4 million years. *Nature*  
662 *Communications*, 7, 10325, doi: 10/1038/ncomms10325, 2016.

663

664 Hodge, R., Brasington, J., and Richards, K.: In-situ characterisation of grain-scale  
665 fluvial morphology using Terrestrial Laser Scanning. *Earth Surface Processes and*  
666 *Landforms*, 34, 954-968, doi: 10.1002/esp.1780, 2009.

667

668 Immerzeel, W. W., Kraaijenbrink, P. D. A., Shea, J. M., Shrestha, A. B., Pellicciotti,  
669 F., Bierkens, M. F. P., and de Jong, S. M.: High-resolution monitoring of Himalayan  
670 glacier dynamics using unmanned aerial vehicles. *Remote Sensing of Environment*,  
671 150, 93-103, doi: 10.1016/j.rse.2014.04.025, 2014.

672

673 Irvine-Fynn, T. D. L., Sanz-Ablanedo, E., Rutter, N., Smith, M. W., and Chandler, J.  
674 H.: Measuring glacier surface roughness using plot-scale, close-range digital  
675 photogrammetry. *Journal of Glaciology*, 60(223), 957-969, doi:  
676 10.3189/2014JoG14J032, 2014.

677

678 James, M. R., and Robson, S.: Straightforward reconstruction of 3D surfaces and  
679 topography with a camera: accuracy and geoscience application. *Journal of*  
680 *Geophysical Research*, 117, F03017, doi: 10.1029/2011JF002289, 2012.

681

682 James, M. R. and Robson, S.: Mitigating systematic error in topographic models  
683 derived from UAV and ground-based image networks. *Earth Surface Processes and*  
684 *Landforms*, 39, 1413-1420, doi: 10.1002/esp.3609, 2014.

685  
686 James, M. R., Robson, S., Pinkerton, H., and Ball, M.: Oblique photogrammetry with  
687 visible and thermal images of active lava flows. *Bulletin of Volcanology*, 69, 105-108,  
688 doi: 10.1007/200445-006-0062-9, 2006.

689  
690 Javernick, L., Brasington, J., and Caruso, B.: Modelling the topography of shallow  
691 braided rivers using Structure-from-Motion photogrammetry. *Geomorphology*, 213,  
692 116-182, doi: 10.1016/j.geomorph.2014.01.006, 2014.

693  
694 Kääb, A.: Monitoring high-mountain terrain deformation from repeated air- and  
695 spaceborne optical data: examples using digital aerial imagery and ASTER data.  
696 *ISPRS Journal of Photogrammetry and Remote Sensing*, 57(1-2), 39-52, doi:  
697 10.1016/S0924-2716(02)00114-4, 2002.

698  
699 Kääb, A., Girod, L., and Berthling, L.: Surface kinematics of periglacial sorted circles  
700 using structure-from-motion technology. *The Cryosphere*, 8, 1041-1056, doi:  
701 10.5194/tc-8-1041-2014, 2014.

702  
703 Keim, R. F., Skaugset, A. E., and Bateman, D. S.: Digital terrain modelling of small  
704 stream channels with a total-station theodolite. *Advances in Water Resources*, 23,  
705 41-48, doi: 10.1016/S0309-1708(99)00007-X, 1999.

706  
707 Keutterling, A. and Thomas, A.: Monitoring glacier elevation and volume changes  
708 with digital photogrammetry and GIS at Gepatschferner glacier, Austria. *International*  
709 *Journal of Remote Sensing*, 27(19), 4371-4380, doi: 10.1080/01431160600851819,  
710 2006.

711  
712 Kraaijenbrink, P., Meijer, S. W., Shea, J. M., Pellicciotti, F., de Jong, S. M., and  
713 Immerzeel W. W.: Seasonal surface velocities of a Himalayan glacier derived by  
714 automated correlation of unmanned aerial vehicle imagery. *Annals of Glaciology*,  
715 57(71), 103-113, doi: 10.3189/2016AoG71A072, 2016.

716  
717 Krüger, J., and Kjær, K.H.: De-icing progression of ice-cored moraines in a humid,  
718 subpolar climate, Kötlujökull, Iceland. *The Holocene*, 10(6), 737-747, doi:  
719 10.1191/09596830094980, 2000.

720  
721 Lague, D., Brodu, N., and Leroux, J.: Accurate 3D comparison of complex  
722 topography with terrestrial laser scanner: Application to the Rangitikei canyon (N-Z).  
723 *ISPRS Journal of Photogrammetry and Remote Sensing*, 82, 10-26, doi:  
724 10.1016/j.isprsjprs.2013.04.009, 2013.

725  
726 Lewis, A., Hilley, G. E., and Lewicki, J. L.: Integrated thermal infrared imaging and  
727 structure-from-motion photogrammetry to map apparent temperature and radiant  
728 hydrothermal heat flux at Mammoth Mountain, CA, USA. *Journal of Volcanology and*  
729 *Geothermal Research*, 303, 16-24, doi: 10.1016/j.jvolgeores.2015.07.025, 2015.

730

731 Lowe, D. G.: Distinctive image features from scale-invariant keypoints. *International*  
732 *Journal of Computer Vision*, 60(2), 91-110, doi:  
733 10.1023/B%VISI.0000029664.99615.94, 2004.  
734

735 Micheletti, N., Chandler, J. H., and Lane, S. N.: Investigating the geomorphological  
736 potential of freely available and accessible structure-from-motion photogrammetry  
737 using a smartphone. *Earth Surface Processes and Landforms*, 40(4), 473-486, doi:  
738 10.1002/esp.3648, 2014.  
739

740 Micheletti, N., Lane, S. N., and Chandler, J. H.: Application of archival aerial  
741 photogrammetry to quantify climate forcing of Alpine landscapes. *The*  
742 *Photogrammetric Record*, 30(150), 143-165, doi: 10.1111/phor.12099, 2015.  
743

744 Milan, D. J., Heritage, G. L., and Hetherington, D.: Application of a 3D laser scanner  
745 in the assessment of erosion and deposition volumes and channel change in a  
746 proglacial river. *Earth Surface Processes and Landforms*, 32, 1657-1674, doi:  
747 10.1002/esp.1592, 2007.  
748

749 Niethammer, U., Rothmund, S., James, M. R., Traveletti, J., and Joswig, M.: UAV-  
750 based remote sensing of landslide. *International Archives of the Photogrammetry,*  
751 *Remote Sensing and Spatial Information Sciences*, 38(5), 496-501, doi:  
752 10.1016/j.enggeo.2011.03.012, 2010.  
753

754 Noh, M-J. and Howat, I. M.: Automated stereo-photogrammetric DEM generation at  
755 high latitudes: Surface Extraction with TIN-based Search-space Minimization  
756 (SETSM) validation and demonstration over glaciated regions. *GIScience and*  
757 *Remote Sensing*, 52(2), doi: 10.1080/15481603.2015.1008621, 198-217, 2015.  
758

759 Ouédraogo, M. M., Degré, A., Debouche, C., and Lisein, J.: The evaluation of  
760 unmanned aerial system-based photogrammetry and terrestrial laser scanning to  
761 generate DEMs of agricultural watersheds. *Geomorphology*, 214, 339-355, doi:  
762 10.1016/j.geomorph.2014.02.016, 2014.  
763

764 Passalacqua, P., Hillier, J., and Tarolli, P.: Innovative analysis and use of high-  
765 resolution DTMs for quantitative interrogation of Earth-surface processes. *Earth*  
766 *Surface Processes and Landforms*, 39, 1400-1403, doi: 10.1002/esp.3616, 2014.  
767

768 Passalacqua, P., Belmont, P., Staley, D. M., Simley, J. D., Arrowsmith, J. R., Bode,  
769 C. A., Crosby, C., DeLong, S. B., Glenn, N. F., Kelly, S. A., Lague, D., Sangireddy,  
770 H., Schaffrath, K., Tarboton, D. G., Wasklewicz, T., and Wheaton, J. M.: Analyzing  
771 high resolution topography for advancing the understanding of mass and energy  
772 transfer through landscapes: A review. *Earth-Science Reviews*, 148, 174-193, doi:  
773 10.1016/j.earscirev.2015.05.012, 2015.  
774

775 Pepin, N. C., Duane, W. J., Schaefer, M., Pike, G., and Hardy, D. R.: Measuring and  
776 modeling the retreat of the summit ice fields on Kilimanjaro, East Africa. *Arctic,*  
777 *Antarctic and Alpine Research*, 46(4), 905-917, doi: 10.1657/1938-4246-46.4.905,  
778 2014.  
779

780 Piermattei, L., Carturan, L., and Guarnieri, A.: Use of terrestrial photogrammetry  
781 based on structure-from-motion for mass balance estimation of a small glacier in the  
782 Italian alps. *Earth Surface Processes and Landforms*, 40, 1791-1802, doi:  
783 10.1002/esp.3756, 2015.

784

785 Pitkänen, T. and Kajuutti, K.: Close-range photogrammetry as a tool in glacier  
786 change detection. *International Archives of the Photogrammetry, Remote Sensing*  
787 *and Spatial Information Sciences (ISPRS)*, 35, 769-773, 2004.

788

789 Reid, T. D., Carenzo, M., Pellicciotti, F., and Brock, B. W.: Including debris cover  
790 effects in a distributed model of glacier ablation. *Journal of Geophysical Research:*  
791 *Atmospheres*, 117, D18105, doi: 10.1029/2012JD017795, 2012.

792

793 Rippin, D. M., Pomfret, A., and King, N.: High resolution mapping of supra-glacial  
794 drainage pathways reveals links between micro-channel drainage density, surface  
795 roughness and surface reflectance. *Earth Surface Processes and Landforms*,  
796 40(10), 1279-1290, doi: 10.1002/esp.3719, 2015.

797

798 Rosnell, T. and Honkavaara, E.: Point cloud generation from aerial image data  
799 acquired by a quadcopter type micro unmanned aerial vehicle and a digital still  
800 camera. *Sensors*, 12, 453-480, doi: 10.3390/s120100453, 2012.

801

802 Rosser, N. J., Petley, D. N., Lim, M., Dunning, S. A., and Allison, R. J.: Terrestrial  
803 laser scanning for monitoring the process of hard rock coastal cliff erosion. *Quarterly*  
804 *Journal of Engineering Geology & Hydrogeology*, 38, 363-375, 2005.

805

806 Ryan, J. C., Hubbard, A. L., Box, J. E., Todd, J., Christoffersen, P., Carr, J. R., Holt,  
807 T. O., and Snooke, N.: UAV photogrammetry and structure from motion to assess  
808 calving dynamics at Store Glacier, a large outlet draining the Greenland ice sheet.  
809 *The Cryosphere*, 9, 1-11, doi: 10.5194/tc-9-1-2015, 2015.

810

811 Sanz-Ablanedo, E., Chandler, J. H., and Irvine-Fynn, T. D. L.: Studying glacial melt  
812 processes using sub-centimeter DEM extraction and digital close-range  
813 photogrammetry. *ISPRS Archives*, 39(B5), 435-440, 2012.

814

815 Schomacker, A.: What controls dead-ice melting under different climate conditions?  
816 A discussion. *Earth-Science Reviews*, 90, 103-113, doi:  
817 10.1016/j.earscirev.2008.08.003, 2008.

818

819 Schwalbe, E. and Maas, H. G.: Motion analysis of fast flowing glaciers from multi-  
820 temporal terrestrial laser scanning. *Photogrammetrie Fernerkundung*  
821 *Geoinformation*, 1, 91-98, doi: 10.1127/0935-1221/2009/0009, 2009.

822

823 Sinisalo, A. and Moore, J. C.: Antarctic blue ice area – towards extracting  
824 paleoclimate information. *Antarctic Science*, 22(2), 99-115, doi:  
825 10.107/S0954102009990691, 2010.

826

827 Smith, M. J., Rose, J., and Booth, S.: Geomorphological mapping of glacial  
828 landforms from remotely sensed data: An evaluation of the principal data sources

829 and an assessment of their quality. *Geomorphology*, 76(1-2), 148-165, doi:  
830 10.1016/j.geomorph.2005.11.001, 2006.

831

832 Smith, M. J., Rose, J., and Gousie, M. B.: The Cookie Cutter: A method for obtaining  
833 a quantitative 3D description of glacial bedforms. *Geomorphology*, 108, 209-218, doi:  
834 10.1016/j.geomorph.2009.01.006, 2009.

835

836 Smith, M. W. and Vericat, D.: From experimental plots to experiment landscapes:  
837 topography, erosion and deposition in sub-humid badlands from Structure-from-  
838 Motion photogrammetry. *Earth Surface Processes and Landforms*, doi:  
839 10.1002/esp.3747, 2015.

840

841 Spaulding, N. E., Spikes, V. B., Hamilton, G. S., Mayewski, P. A., Dunbar, N. W.,  
842 Harvey, R. P., Schutt, J., and Kurbatov, A. V.: Ice motion and mass balance at the  
843 Allan Hills blue-ice area, Antarctica, with implications for paleoclimate  
844 reconstructions. *Journal of Glaciology*, 58(208), 399-406, doi:  
845 10.3189/2012JoG11J176, 2012.

846

847 Staines, K. E. H., Carrivick, J. L., Tweed, F. S., Evans, A. J., Russell, A. J.,  
848 Jóhannesson, T., and Roberts, M.: A multi-dimensional analysis of pro-glacial  
849 landscape change at Sólheimajökull, southern Iceland. *Earth Surface Processes and*  
850 *Landforms*, 40, 809-822, doi: 10.1002/esp.3662, 2015.

851

852 Stumpf, A., Malet, J-P., Allemand, P., and Ulrich, P.: Surface reconstruction and  
853 landslide displacement measurements with Pléiades satellite images. *ISPRS Journal*  
854 *of Photogrammetry and Remote Sensing*, 95, 1-12, doi:  
855 10.1016/j.isprsjprs.2014.05.008, 2014.

856

857 Tarolli, P.: High-resolution topography for understanding Earth surface processes:  
858 Opportunities and challenges. *Geomorphology*, 216, 295-312, doi:  
859 10.1016/j.geomorph.2014.03.008, 2014.

860

861 Tonkin, T. N., Midgley, N. G., Graham, D. J., and Labadz, J. C.: The potential of  
862 small unmanned aircraft systems and structure-from-motion for topographic surveys:  
863 a test of emerging integrated approaches at Cwm Idwal, North Wales.  
864 *Geomorphology*, 226, 35-43, doi: 10.1016/j.geomorph.2014.07.021, 2014.

865

866 Vieira, R., Hinata, S., da Rosa, K. K., Zilberstein, S., and Simoes, J. C.: Periglacial  
867 features in Patriot Hills, Ellsworth Mountains, Antarctica. *Geomorphology*, 155-156,  
868 96-101, doi: 10.1016/j.geomorph.2011.12.014, 2012.

869

870 Westoby, M. J., Brasington, J., Glasser, N. F., Hambrey, M. J., and Reynolds, J. M.:  
871 'Structure-from-Motion' photogrammetry: A low-cost, effective tool for geoscience  
872 applications. *Geomorphology*, 179, 300-314, doi: 10.1016/j.geomorph.2012.08.021,  
873 2012.

874

875 Westoby, M. J., Dunning, S. A., Woodward, J., Hein, A. S., Marrero, S. M., Winter,  
876 K., and Sugden, D. E.: Sedimentological characterisation of Antarctic moraines  
877 using UAVs and Structure-from-Motion photogrammetry. *Journal of Glaciology*,  
878 61(230), 1088-1102, doi: 10.3189/2015JoG15J086, 2015.

879

880 Wheaton, J. M., Brasington, J., Darby, S. E., and Sear, D. A.: Accounting for  
881 uncertainty in DEMs from repeat topographic surveys: improved sediment budgets.  
882 *Earth Surface Processes and Landforms*, 35, 136-156, doi: 10.1002/esp.1886, 2010.

883

884 Whitehead, K., Moorman, B., and Wainstein, P.: Measuring daily surface elevation  
885 and velocity variations across a polythermal arctic glacier using ground-based  
886 photogrammetry. *Journal of Glaciology*, 60(224), 1208-1220, doi:  
887 10.3189/2014JoG14J080, 2014.

888

889 Woodget, A. S., Carbonneau, P. E., Visser, F., and Maddock, I. P.; Quantifying  
890 submerged fluvial topography using hyperspatial resolution UAS imagery and  
891 structure from motion photogrammetry. *Earth Surface Processes and Landforms*,  
892 40(1), 47-64, doi: 10.1002/esp.3613, 2015.

893

894 **Figure captions**

895

896 **Figure 1.** Blue-ice moraine embayment, Patriot Hills, Heritage Range, Antarctica. **(a)**  
897 Geographical context of Patriot Hills within the Heritage Range, southern Ellsworth  
898 Mountains.**(b)** The Patriot Hills massif. The location of the study embayment and  
899 area displayed in **(c)** is highlighted in red. **(c)**: Detailed study site overview map.  
900 Contours and underlying hillshade are derived from a UAV-SfM-derived DEM. TLS  
901 positions for the start of season 1 are shown in red, blue and yellow. The two scan  
902 positions re-occupied at the end of season 1 are shown in blue, whilst the three scan  
903 positions reoccupied in season 2 are shown in blue and red. Background to **(a)** ©  
904 U.S. Geological Survey, **(b)** 2015 DigitalGlobe, both extracted from Google Earth.

905

906 **Figure 2.** Field photographs of the Patriot Hills blue-ice moraine study site. **(a)**  
907 Panoramic photograph of the moraine embayment – view north-east towards the ice  
908 margin from the rear of the embayment. Area shown in **(c)** and position and view  
909 direction of camera **(b)** shown for reference. **(b)** View to the north-west with moraine  
910 crest in foreground and subdued, ice-marginal moraine surface topography in  
911 middle-ground. **(c)** Close-up of moraine topography, highlighting ridges and furrows  
912 on moraine crests and in inter-moraine troughs.

913

914 **Figure 3.** Results of vertical ( $Z_{diff}$ ; m) differencing of the UAV-SfM and TLS datasets  
915 acquired at the end of season 1, represented as the mean difference within  $10\text{ m}^2$   
916 grid cells. 83% of the UAV-SfM data were found to be within  $\pm 0.1\text{ m}$  of the equivalent  
917 TLS data. Profiles A-C are displayed in Fig. 4.

918

919 **Figure 4.** Moraine surface elevation profiles, extracted from gridded ( $0.2\text{ m}^2$ ) digital  
920 elevation models of TLS- and SfM-derived topographic datasets. Profile locations are  
921 shown in Figures 3 and 6. Profiles A and B bisect the main central moraine crest,  
922 whilst profile C is located on moraine deposits at the back of the embayment. Inset  
923 numbered boxes in profiles A and C show areas referred to in the text.

924

925 **Figure 5.** Vertical component of 3D topographic change ( $Z_{diff}$ ) overlain on a UAV-  
926 SfM-derived hill-shaded DEM of the Patriot Hills blue-ice moraine complex.  
927 Topographic evolution was quantified using the Multiscale Model to Model Cloud  
928 Comparison (M3C2) algorithm in CloudCompare software. Vertical change is  
929 represented as the mean of significant change beyond a threshold of  $\pm 0.103\text{ m}$   
930 within  $10\text{ m}^2$  grid cells. **(a)** UAV-SfM orthophotograph of the study site. Panels **(b)** to  
931 **(f)** cover specific differencing epochs using a combination of TLS and SfM data (see  
932 panel headings). Dashed line in **(b)** to **(f)** indicates locations of primary moraine ridge  
933 crest.

934

935 **Figure 6.** Change detection mapping for **(a,b)** intra-annual (season 1 start to season  
936 1 end) and **(c)** annual (season 1 start to season 2) differencing epochs. Horizontal  
937 difference vectors ( $XY_{diff}$ ) are scaled by magnitude and oriented according to the

938 direction of change. The vertical component of 3D change ( $Z_{diff}$ ) is shown in the  
939 background. Transects A-C denote the location of moraine surface profiles displayed  
940 in Fig. 3 and Fig. 4. Red dashes on all panels shows the approximate location of  
941 primary moraine ridge crest.

942

943 **Table 1.** Terrestrial laser scanning and UAV-SfM survey dates and registration  
944 errors. Within each season, individual scans were registered to a single static  
945 position to produce a single, merged point cloud (scan-scan registration error). TLS  
946 data from the end of season 1 and for season 2 were subsequently registered to TLS  
947 data acquired at the start of season 1, producing a project-project registration error.  
948 The UAV-SfM data (season 1 end) were registered to TLS data from the end of  
949 season 1.

950

951 **Table 2.** Registration error propagation for specific differencing epochs. The  
952 propagated error for each differencing epoch is calculated using Eq. 3. The 95%  
953 level of detection, or detection threshold is calculated in M3C2 as the product of the  
954 propagated error and a measure of local point cloud roughness (Lague et al., 2013).  
955 The results of 3D differencing were filtered in CloudCompare so that only differences  
956 largest than the most conservative (largest)  $LoD_{95\%}$  (i.e. 0.103 m) were considered to  
957 represent significant change.



<b>Field survey</b>	<b>Scan position</b>	<b>Scan date</b>	<b>Scan-scan registration error (RMS; m)</b>	<b>Project-project registration error (RMS; m)</b>
Season 1 start (TLS)	1	07 Dec 2012	Static	Static
	2	08 Dec 2012	0.0327	
	3	08 Dec 2012	0.0391	
	5	09 Dec 2012	0.0301	
	6	01 Dec 2012	0.0258	
	7	11 Dec 2012	0.0258	
	Season 1 end (TLS)	1	09 Jan 2013	Static
2		09 Jan 2013	0.0145	
Season 1 end (UAV-SfM)	-	05 Jan 2013	-	0.0306
Season 2 (TLS)	1	14 Jan 2014	Static	0.0149
	2	14 Jan 2014	0.0205	
	3	14 Jan 2014	0.0255	

959 **Table 2**  
960

<b>Differencing epoch</b>	<b>Propagated error (RMS; m)</b>	<b>M3C2 <math>LoD_{95\%}</math> (m)</b>
S1 start (TLS) - S1 end (TLS)	0.049	0.098
S1 start (TLS) - S1 end (SfM)	0.050	0.103
S1 end (TLS) - S2 end (TLS)	0.048	0.098
S1 end (SfM) - S2 end (TLS)	0.049	0.102
S1 start (TLS) - S2 end (TLS)	0.050	0.099

**Figure 1**

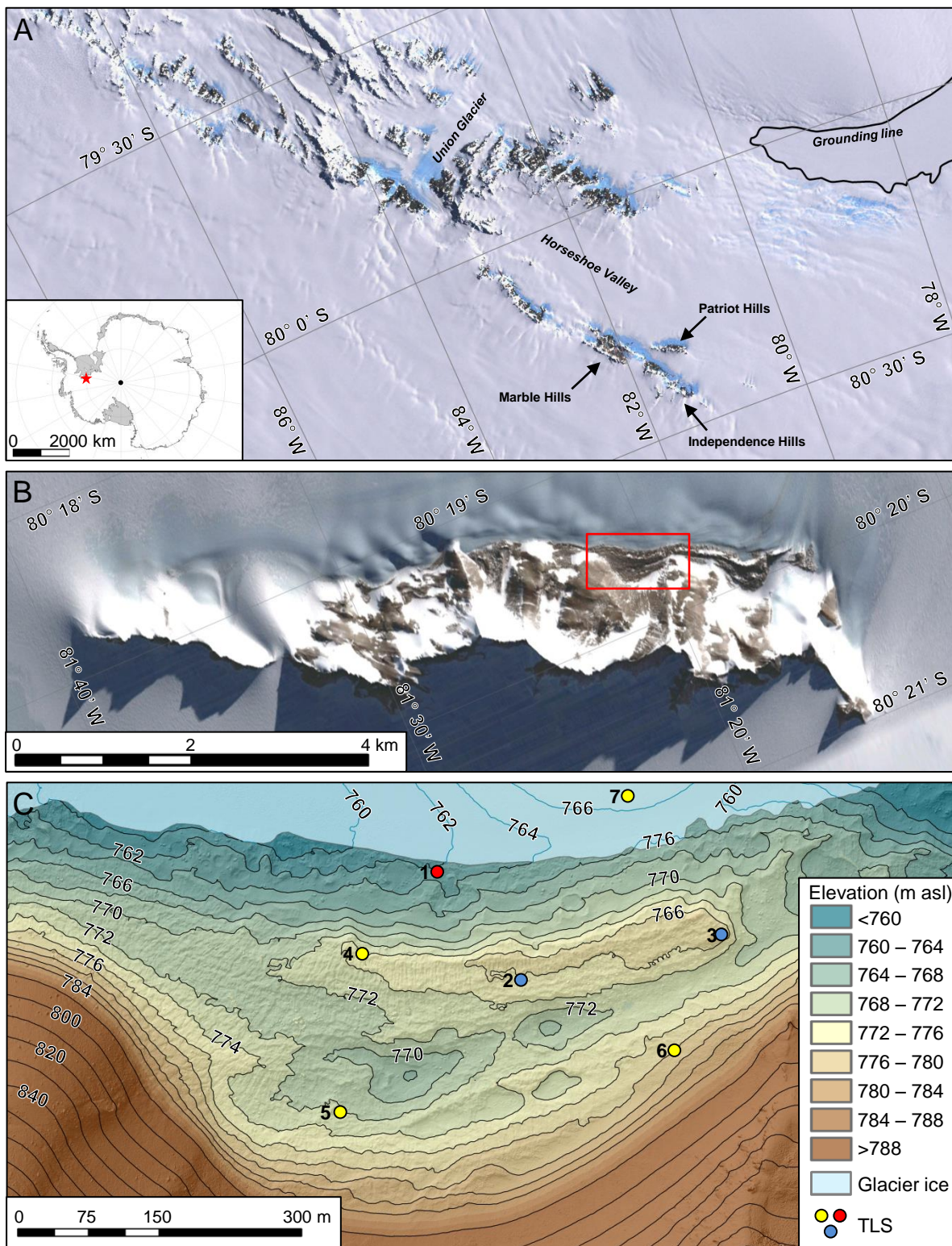


Figure 2

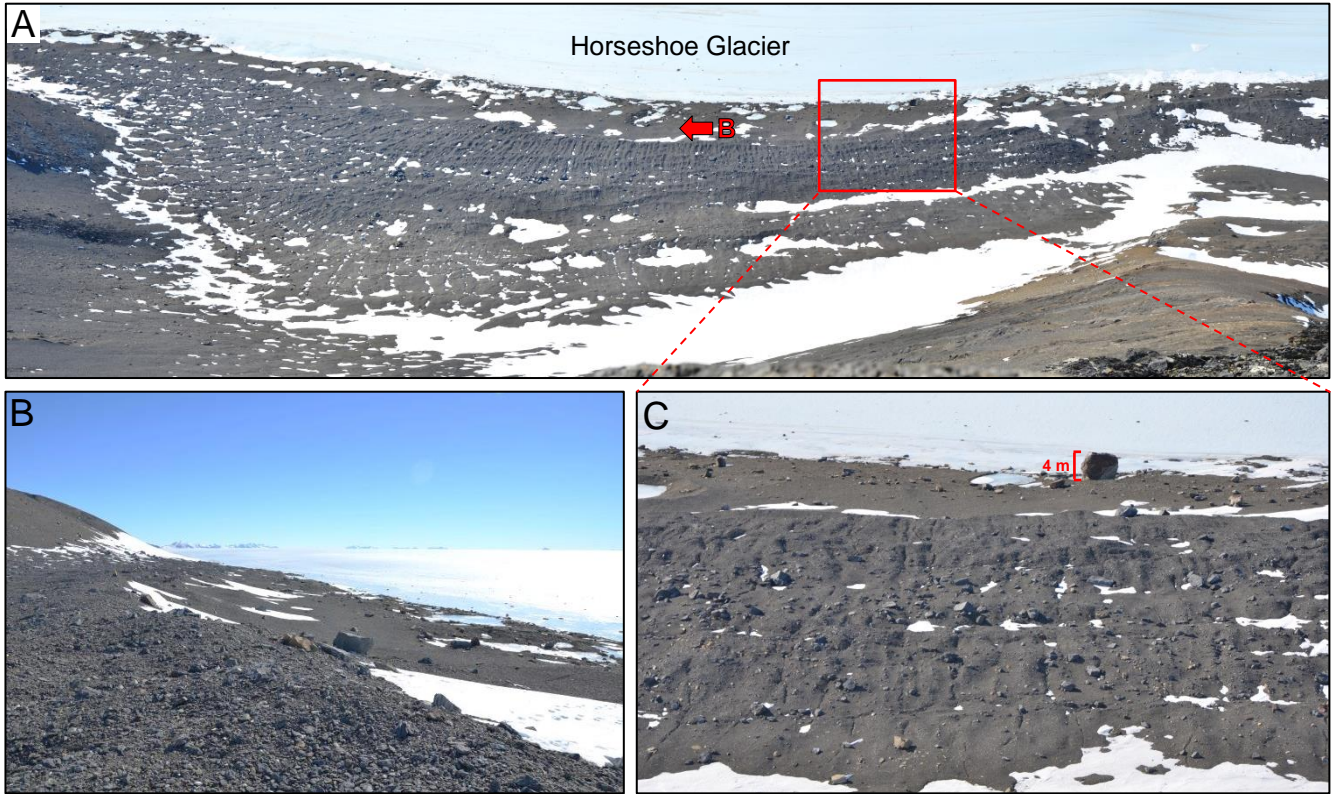




Figure 3

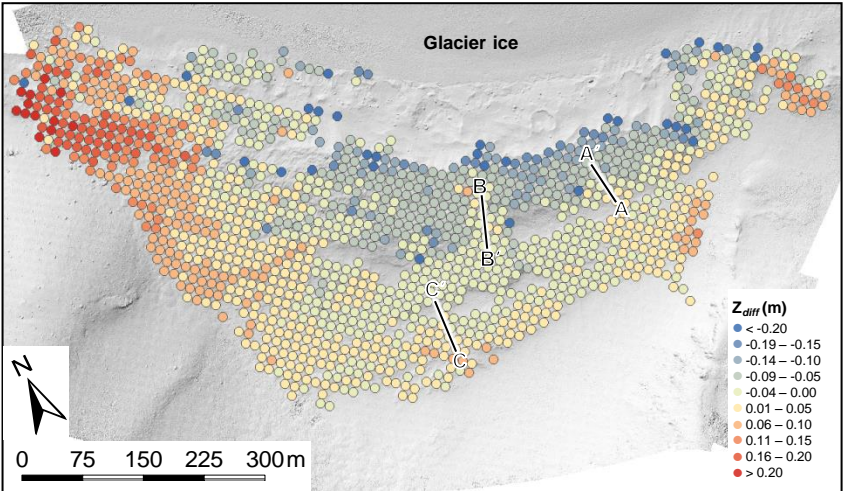
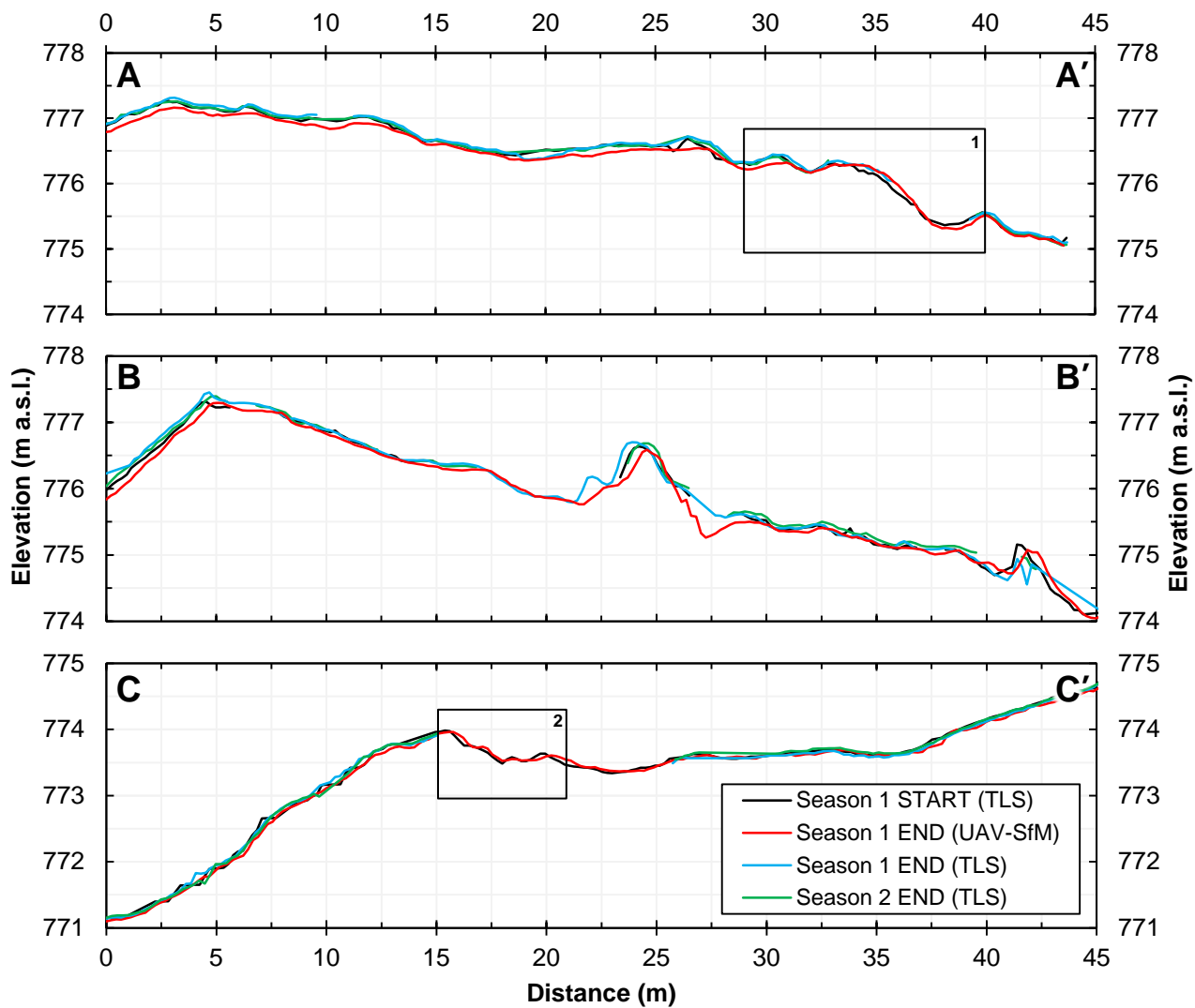


Figure 4



**Figure 5**

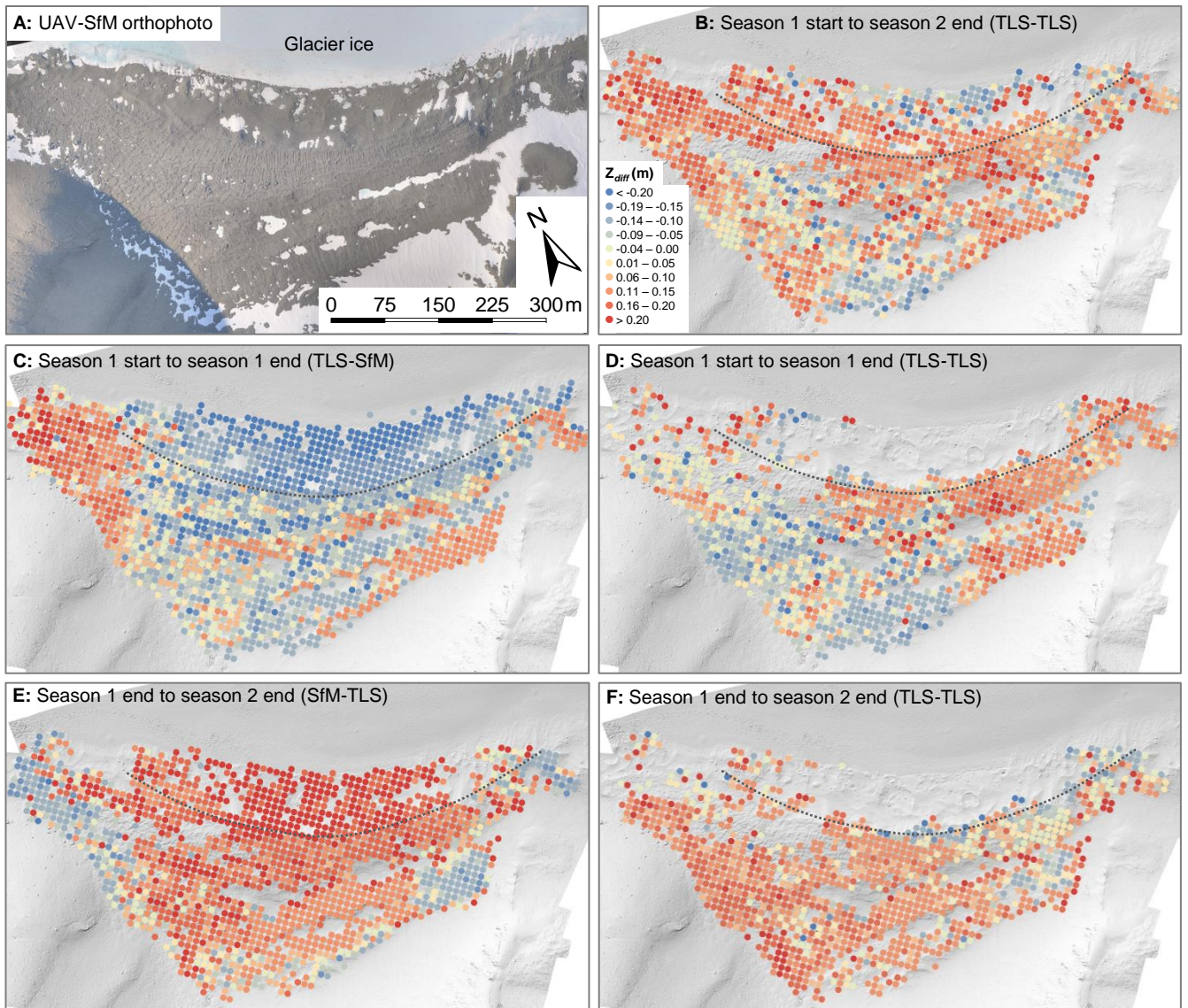




Figure 6

